

A New View into the Silica Deposition Vesicles of Diatoms

Christoph Heintze

Technische Universität Dresden

Petr Formanek

Leibniz-Institut für Polymerforschung Dresden e. V.

Darius Pohl

Technische Universität Dresden

Jannes Hauptstein

Technische Universität Dresden

Bernd Rellinghaus

Technische Universität Dresden

Nils Kröger (✉ nils.kroeger@tu-dresden.de)

Technische Universität Dresden <https://orcid.org/0000-0002-8115-4129>

Research article

Keywords: Thalassiosira pseudonana, Cyclotella cryptica, biosilica, morphogenesis, cell wall, costa, cribrum pore, areola pore, fultoportula, silica nanoparticle

Posted Date: April 27th, 2020

DOI: <https://doi.org/10.21203/rs.3.rs-22354/v1>

License:  This work is licensed under a Creative Commons Attribution 4.0 International License.

[Read Full License](#)

Version of Record: A version of this preprint was published on August 28th, 2020. See the published version at <https://doi.org/10.1186/s42833-020-00017-8>.

Abstract

Diatoms are single-celled microalgae that produce silica-based cell walls with intricate nano- and micropatterns. Biogenesis of diatom biosilica is a bottom-up process that occurs in large intracellular compartments termed silica deposition vesicles (SDVs). Investigating the mechanism of silica morphogenesis has so far been severely limited by the lack of methods for imaging the entire volume of an SDV with high spatial resolution during all stages of development. Here we have developed a method that allows for rapid identification and electron microscopy imaging of many different, full sized SDVs that are in the process of producing biosilica valves. This enabled visualizing the development of characteristic morphological biosilica features with unprecedented spatio-temporal resolution. During early to mid-term development, valve SDVs contained ~ 20 nm sized particles that were primarily associated with the radially expanding rib-like biosilica structures. The results from electron dispersive X-ray analysis suggests that the immature biosilica patterns are silica-organic composites. This supports the hypothesis that silica morphogenesis is dependent on organic biomolecules inside the SDV lumen.

Introduction

Diatoms are a species-rich lineage of single-celled algae that produce silica-based cell walls with species-specific morphologies. A characteristic feature of diatom biosilica are hierarchical patterns of pores with diameters from the nano- to the micrometer range. The porous patterns equip diatom biosilica with interesting materials properties, such as light capturing and the highest specific strength of any known biological material (1–9). A rapidly increasing number of genome and transcriptome data from diatoms has become available, and several species are readily amenable to genetic manipulation (10). Therefore diatoms are the prime model systems for studying the molecular basis of biological silica formation, and has enabled genetic engineering methods to further enhance the functionalities of diatom biosilica (7, 11, 12).

Diatom cell walls are constructed from two types of biosilica building blocks termed valves and girdle bands. In the cylindrical cell walls of *Thalassiosira pseudonana* and *Cyclotella cryptica*, which have been studied in the present work, the valves represent the top and bottom lids of the cylinder. The girdle bands are partially overlapping rings of silica that are oriented transversely to the long axis of the cylinder constituting a gap-less connection between the two valves. Regarding the nano- and microarchitecture, the biosilica of valves is much more intricately patterned including hierarchical pore patterns, struts, and tubes, while girdle bands, in most cases, are flat and perforated rings. Biogenesis of the valves and girdle bands is tightly linked to the cell cycle with valves only being produced during cell division, while girdle bands are made exclusively during interphase. Each valve and each girdle band develops inside the cell in a separate compartment termed silica deposition vesicle (SDV). When the formation of an entire valve or girdle band is complete inside its SDV, it is exocytosed to the cell surface and becomes incorporated into the cell wall.

Cell biologists and materials scientist alike have been intrigued by the capability of SDVs to produce intricately patterned biosilica structures (13,14). Several models have been put forward regarding the mechanisms for silica morphogenesis in valve SDVs (13–25). Some models proposed that silica nanoparticles are the building material for biosilica morphogenesis (22, 23), and that proteins and other biomacromolecules in the SDV lumen act as templates in this process (17, 19, 22). However, the presence of silica nanoparticles and biomacromolecular templates inside the SDV has not been demonstrated yet. Furthermore, none of the current models is able to explain biosilica morphogenesis in its entirety.

A major bottleneck for elucidating the mechanism of biosilica morphogenesis is the lack of detailed structural information about all intermediate stages of biosilica development. Previous attempts took advantage of the possibility to synchronize the diatom cell cycle thereby increasing the fraction of cells with developing SDVs. To allow for the imaging of nanoscale features mainly electron microscopy and in a few cases atomic force microscopy (AFM) was employed. Access to the developing biosilica structures inside the intracellular SDVs was achieved by two methods. The first method involved cell lysis using strong acids or detergent, which also removed all or most organic material, and allowed for imaging of the immature biosilica by transmission electron microscopy (TEM), scanning electron microscopy (SEM), and AFM (26–29). As a result, images of the entire volumes of developing biosilica structure, primarily from valves, were obtained. However, the treatment with acid or detergent was prone to introducing artifacts by destroying the SDV membrane and extracting all material from the SDV lumen that is soluble under these conditions. The second method used chemical fixation of cells followed by resin embedment, ultrathin sectioning, and imaging with TEM (30–36). This allowed for imaging developing biosilica inside the SDV and within the entire cellular context. However, the required chemical treatment is susceptible to introducing artifacts, and imaging substantial fractions or an entire SDV volume has not yet been achieved with this method.

Here, we have investigated the possibility to prepare, rapidly identify, and image by TEM intact valve SDVs from cell lysates of the diatoms *Thalassiosira pseudonana* and *Cyclotella cryptica*. The two diatom species are phylogenetically closely related (Order *Thalassiosirales*), have previously been studied regarding their molecular and cellular mechanisms of silica morphogenesis (12, 17, 28, 29), their genome sequences are available (37, 38) and molecular genetic transformation systems have been established (39, 40). By comparing the development of the valves in these two model diatom species, we aimed to identify common steps in biosilica morphogenesis of the *Thalassiosirales*.

Results And Discussion

Identifying valve SDVs in cell lysates

For the rapid identification of valve SDVs in cell lysates, we aimed to establish a fluorescent labeling strategy in combination with correlative fluorescence-electron microscopy imaging, which is outlined in the following. To facilitate following the cell cycle progression *in vivo*, transgenic cell lines were used that expressed C-terminally tagged silicanin-1 (Sin1-GFP^C), which was previously shown to be located in the

membrane of *T. pseudonana* valve and girdle band SDVs (41). By synchronizing the cell culture, the proportion of cells undergoing valve SDV development was enhanced. When the maximum proportion of valve SDV bearing cells was observed, the SDV-specific dye PDMPO was briefly added to the culture to label the silica inside SDVs (42) before it was exocytosed. Cells were gently lysed and the lysate immobilized on a TEM finder grid allowing to rapidly identify the positions of valve SDVs by fluorescence microscopy searching for PDMPO-labeled structures with plate-like morphology. TEM was then employed for imaging the objects at the identified positions.

A Sin1-GFP^C expressing *T. pseudonana* cell line had previously been generated (41), but a corresponding transgenic *C. cryptica* cell line had to be established here. Previously, gene *g20669.t1* had been identified as *Sin1* homologue of *C. cryptica*, because its predicted protein sequence, ccSin1, showed 75.9% global sequence identity to *T. pseudonana* Sin1 (41). A transgenic *C. cryptica* cell line was produced that expressed C-terminally GFP-tagged ccSin1 (ccSin1-GFP^C) under control of the *ccSin1* promoter and terminator sequences. Fluorescence microscopy revealed that ccSin1-GFP^C was located in both valve SDVs and girdle band SDVs as well as several other intracellular vesicles (Fig. 1B). These locations match those previously described for Sin1-GFP^C in *T. pseudonana* (Fig. 1A) (41). Based on the sequence and intracellular location, we concluded that ccSin1 indeed represents the functional homologue of *T. pseudonana* Sin1.

Previously, incubation of diatom cultures in silicon-free medium for extended period of times followed by replenishment of silicic acid (in the following abbreviated Si) has achieved only partial cell cycle synchrony for various diatoms species including *T. pseudonana* and *C. cryptica* (29, 43). Here, we have investigated the effect of two consecutive Si starvation-replenishment series on the synchrony of cell division in *T. pseudonana* and *C. cryptica*. During the first Si starvation-replenishment series for *T. pseudonana*, an increase in cell density occurred 2.5 hours after re-addition of Si (Fig. 1C, black dots). The initial cell density had doubled after 5.5 hours, which suggested that each cell underwent one cell division within 3 hours. The percentage of dividing cells at several time points after Si replenishment was estimated based on the proportion of cells that exhibited the characteristic valve-shaped Sin1-GFP^C fluorescence in the mid cell region (at each time point 100 cells were examined). The maximum proportion of cells containing valve SDVs was ~ 30% and was observed 3.5 hours after replenishment of Si. After 9 hours, the cells were subjected again to Si starvation followed by Si replenishment. This time, the cell number doubled between 2.75-5 hours after Si replenishment and thus required only 2.25 hours (Fig. 1C, blue dots). The maximum proportion of dividing cells was 70% and was reached 3 hours after Si replenishment. These data demonstrated that the two consecutive silicon starvation-replenishment series improved the cell division synchrony in *T. pseudonana*. In contrast, for *C. cryptica* one Si starvation-replenishment series achieved better cell cycle synchrony than two consecutive ones. In the first series, cell division started 4.75 hours after Si replenishment, and the cell density had doubled after 10 hours (Fig. 1D, black dots). The maximum proportion of dividing cells was observed 5.5 hours after Si replenishment and was only 10%. During the second silicon starvation-replenishment cycle, the cell density increased only 50% within 12 hours after Si replenishment, and the maximum proportion of

dividing cells was only 7% (observed after 6 hours; Fig. 1D, blue dots). We assumed, that repeated Si starvation imposes a higher metabolic stress on *C. cryptica* compared to *T. pseudonana*, and thus the growth rate of the former slows down after the second Si starvation period.

To tag valve SDVs with a second fluorescent label, synchronized cells were incubated briefly (10 min) with PDMPO at the time point when the highest proportion of valve SDV bearing cells was present, i.e., 3 and 5.5 hours after the second Si replenishment for *T. pseudonana* and *C. cryptica*, respectively (Fig. 1C, D; red arrows). Immediately after PDMPO labelling, the cells were gently lysed, and putative valve SDVs could be readily identified by epifluorescence microscopy as GFP and PDMPO labeled disks (Fig. 2A; yellow arrows). Discs that exhibited much stronger contrast in bright field microscopy than the putative valve SDVs but lacked both GFP and PDMPO fluorescence (Fig. 2B; white arrowhead), were presumed to be mature valves. Inspection of many putative valve SDVs revealed differences in diameters and PDMPO fluorescence patterns (Fig. 2B). Discs with diameters of 2–3 μm showed usually a quite homogeneous distribution of PDMPO fluorescence. In contrast, SDVs with diameters of 4–6 μm showed homogeneous fluorescence only in the central region and exhibited a more strongly fluorescent rim with a dot-like pattern. We hypothesized that the different types of PDMPO labeled disks represent valve SDVs containing biosilica at different developmental stages. To verify this, a correlative fluorescence approach and transmission electron approach was applied, which revealed that PDMPO and GFP labeled disks indeed contained immature valve biosilica (Fig. 3).

TEM analysis of valve morphogenesis

To obtain a detailed view of valve morphogenesis, more than 150 TEM images of valve SDVs of different sizes were obtained from *T. pseudonana*. This confirmed that SDVs with a homogenous PDMPO pattern corresponded to earlier developmental stages of the biosilica than those exhibiting intense, dot-patterned PDMPO fluorescence at the rim (Fig. S1). An analogous correlated fluorescence microscopy-TEM analysis was performed with lysates from ccSin1-GFP^C expressing and PDMPO labeled *C. cryptica* cells. From these analyses, the sequence of changes in biosilica structure during valve morphogenesis was reconstructed for both *T. pseudonana* and *C. cryptica* (Figs. 4, 5). The general criterion to establish the sequence of valve development was the progression of individual silica features, such as the dendritic branches, the porous layers or the formation of tube-like structures (called fultoportula). The biosilica features were compared among all valve SDV images to determine the correct order of valve development. In the following, the valve morphogenesis processes of *T. pseudonana* and *C. cryptica* are comparatively described.

In both species, the smallest discernable biosilica structure is a central silica ring (termed annulus) from which regularly spaced, radial silica ribs (termed costae) emerge (Fig. 4A, 5A). The costae start branching relatively soon after they emerge from the annulus. They have rather rough edges and seem to be composed of an agglomeration of globular particles. As the valve SDV increases in diameter, the costae continue to grow radially in both species (Fig. 4B, C). In *C. cryptica* thinner costae (termed narrow costae)

emanate from the much wider primary costae (Fig. 5B). As the SDV diameter increases, the narrow costae grow radially in parallel to the wide costae (Fig. 5C, D).

Already at early stages during costae growth in *T. pseudonana*, the formation of pores with ~ 20 nm diameter (i.e. cribrum pores) occurs in the valve center (Fig. 4C, D). Subsequently, cribrum pore formation propagates radially along the costae and a thin silica layer develops around the pores (Fig. 4D, E) eventually filling the entire space between the costae (Fig. 4F). In *C. cryptica* the formation of cribrum pores that have similar diameters (~ 20 nm) as in *T. pseudonana* also starts in the center relatively early during valve development (Fig. 5C). Cribrum pore formation proceeds radially outward along the wide and narrow costae (Fig. 5C-H). However, as the space between the costae becomes filled with a layer of silica, 1–3 additional rows of cribrum pores are formed that are not adjacent to any costa (Fig. 5H). In contrast, cribrum pores that are not adjacent to costae are quite rare in *T. pseudonana*.

When the costae have almost reached their full length, the formation of regularly spaced, tube-like structures (each termed fultoportula) is initiated in *T. pseudonana*. Fultoportula formation is highly synchronized throughout the valve and involves the ends of four (rarely three) costae, which cease normal growth and instead develop into a central tube with three satellite pores (Fig. 4F-H). The inter costae space adjacent to the fultoportula is fully silicified lacking cribrum pores (Fig. 4G). In the regions between the developing fultoportulae, costae continue to extend but cease shortly after fultoportulae formation is completed. Termination of the lateral valve growth is marked by the merging of the costae ends into a patternless, non-porous ring of silica, which represents a continuous margin of the valve. (Fig. 4H). In *C. cryptica*, each wide costa develops a fultoportula well before the full length of the costae has been reached (Fig. 5E-H). Both wide and narrow costae continue to grow beyond the position of the fultoportulae before they merge into a patternless continuous ring of silica. Both, in *T. pseudonana* and *C. cryptica* almost 50% of the valves contain one (rarely two) fultoportula that is positioned slightly off the valve center (Fig. 4G, H and Fig. 5F-H). Formation of these central fultoportulae always precedes the formation of the fultoportulae at the periphery of the valve (Fig. 4E, 5B).

When fultoportulae formation commences in *T. pseudonana*, neighboring costae in the central part of the valve become connected by silica bridges (Fig. 4F, G). As valve development progresses, the number of silica bridges decreases towards the periphery, however, they become particularly prominent close to the valve margin in the spaces between fultoportulae (Fig. 4H). Two neighboring silica bridges together with the two interjacent costae segments represent so-called areola walls, which together constitute an areola pore. Each areola pore usually encompasses several cribrum pores (Fig. 4F,G).

The formation of fultoportulae and areolae pores coincides with an apparent increase in thickness of the silica throughout the valve, which has previously been coined “z expansion” (28). In *C. cryptica*, the silica bridges between neighboring costae start appearing also during fultoportulae formation (Fig. 5F). Whereas in *T. pseudonana* cribrum pore formation in a given area is always completed before silica bridges arise, both these structural features develop simultaneously in *C. cryptica* (Fig. 5F, G). In some

areas it is evident that an areola pore can be completed even before the cribrum pores are formed (Fig. 5F).

Valve morphogenesis in *T. pseudonana* and *C. cryptica* has been investigated before (28, 29). However, the correlative fluorescence and electron microscopy approach that was established in the present work has enabled the imaging of entire immature valves at an unprecedented number of different developmental stages while they are still encased by the SDV membrane. These include the structures of the annulus and costae at early developmental stages, and the differences between *T. pseudonana* and *C. cryptica* in the timing of the development of cribrum pores and areola pores. Figure 6 schematically summarizes the main steps in the morphogenesis of the valves of *T. pseudonana* and *C. cryptica* to highlight the similarities and differences in structures and development of their valves.

Morphogenesis of cribrum pores in *T. pseudonana*

The cribrum pores of *T. pseudonana* are 22 ± 2 nm ($n = 200$) in diameter and positioned in a seemingly irregular pattern within the silica layer between the costae. In the following we refer to the silica layer between the costae as cribrum pore layer. From numerous images of immature valves at various stages of development, the morphogenesis of the cribrum pore layer was reconstructed (Fig. 7). Cribrum pore formation always starts along the costae, which are initially rather smooth (Fig. 7A, A'; white arrowheads). The costae develop wave-like edges as silica grows into the space between the costae (Fig. 7B, B'; yellow arrowheads). The wave peaks are fairly regularly spaced and each develops into an anvil shaped structure with the anvil ends elongating parallel to the long-axis of the costa (Fig. 7B, B', C; blue arrowheads). The ends of two neighboring anvils that face each other merge, thus establishing a cribrum pore (Fig. 7C, C'; red arrowheads). The rows of cribrum pores associated with neighboring costae usually have very similar periodicities. The space between the two rows of pores becomes filled with silica, when the distance between the costae is < 120 nm. When neighboring costae are spaced wider than 120 nm, additional cribrum pores can develop that do not originate from a costa edge (Fig. 7C; green arrowhead).

The elemental composition of biosilica in valve SDVs

In some of the *T. pseudonana* cell lysate preparations, SDVs were observed that contained many spherical nanoparticles with diameters of 19.4 ± 2.4 nm ($n = 100$) (Fig. 8A-C). The nanoparticles were also observed in some valve SDVs of *C. cryptica* (Fig.S2). In *T. pseudonana*, the nanoparticles were only observed during cribrum pore formation and were primarily associated with the costae. It has previously been hypothesized that silica nanoparticles are the primary building blocks for biosilica morphogenesis inside the SDV (24, 30, 44–47). The hypothesis was based on rather circumstantial evidence, and previous methods for SDV imaging failed to demonstrate the presence of such aggregates inside SDVs. To investigate the elemental composition of the nanoparticles, energy-dispersive X-ray (EDX) spectroscopy was performed. The EDX spectrum of the nanoparticles (Fig. 8D) showed characteristic signals for carbon (0.27 keV), nitrogen (0.40 keV), oxygen (0.52 keV), and silicon (1.75 keV). The silicon and oxygen signals are indicative of the nanoparticles being silica based. The nitrogen signal inside the nanoparticles might hint towards the presence proteins, long-chain polyamines, and/or amino sugar

bearing polysaccharides, all of which are known to be associated with mature diatom biosilica (17–19). However, we cannot rule out that the nitrogen signal originated from nitrogen containing metabolites (e.g., amino acids) or a purely inorganic compound (e.g., nitrate, ammonia). EDX mapping of the valve SDVs confirmed that the costae and the nanoparticles are silica- and nitrogen based (Fig. 8D). The carbon signal in the spectrum originated mainly from the formvar coated grid surface (note that formvar is free of nitrogen and silicon), yet the EDX map clearly indicated the presence of carbon also in the costae (Fig. 8D). This result supports the presence of organic components inside the valve SDV. The silica nanoparticles could not be clearly identified in the carbon map, presumably due to the high carbon signal of the background.

To investigate the elemental composition of the immature valve biosilica independent of the surrounding SDV lipid bilayer and other non-covalently associated components, the lysate was extracted with sodium dodecyl sulfate (SDS) before immobilization on a formvar coated grid. Immature valve biosilica could still be easily identified on the grid, because the PDMPO molecules are tightly incorporated into the silica matrix (42). As expected, the EDX spectrum (Fig. 9) of the detergent-treated, immature valve biosilica showed signals for carbon (0.27 keV), oxygen (0.52 keV), nitrogen, (0.4 keV) and silicon (1.75 keV). Additional signals for cobalt (0.77 keV), aluminum (1.48 keV), and phosphorus (2.0 keV) were obtained. The cobalt signal in the EDX spectrum originated from excitations in the pole piece of the microscope rather than the sample. The presence of aluminum in the immature valve biosilica was not unexpected as this element was previously found in biosilica isolated from both naturally grown and cultivated diatoms (48, 49). Carbon, nitrogen and phosphorous are clearly co-located with the silica in the immature valve, which is consistent with the previously proposed presence of long-chain polyamines and highly phosphorylated proteins (i.e., silaffins and silacidins) (17, 19). The phosphorous signal might also be caused by the presence of inorganic phosphate, which has previously been found associated with mature biosilica in the diatom *Coscinodiscus granii* (50).

Conclusion

In the present study we developed an easy method for labeling and imaging SDVs that should in principle be applicable to all diatoms. A limitation of the method is the sensitivity for PDMPO detection, which makes it difficult to identify very early stages of valve SDVs. The first-time identification of silica nanoparticles inside *T. pseudonana* and *C. cryptica* SDVs, was not entirely unexpected, but was not observed in all preparations. We hypothesize, that the silica nanoparticles may be remnants of highly hydrated liquid nanodroplets that are composed of an intimate mixture of polysilicic acids and organic macromolecules. In SDVs *in vivo*, the Si-organic nanodroplets may provide the material for growth of the costae and the biogenesis of the cribrum plates. The latter develop from the edges of the costae, where the nanoparticles were primarily observed (see. Figure 7). It is conceivable that during relatively uncontrolled drying of our samples, such nanodroplets might often disintegrate or form layers on the costae surfaces rather than yielding spherical nanoparticles. This would explain the inconsistent presence of the silica nanoparticles in our SDV preparations. To finally resolve this question, it will be essential to avoid drying artifacts by performing cryo-EM analysis of valve SDVs.

The EDX analyses provided the first direct demonstration that the biosilica inside SDVs is intimately associated with non-silica components. The C, N and P content of developing biosilica is consistent with the presence of long-chain polyamines and phosphoproteins, which so far have only been located in the mature biosilica of cell walls. Although we regard it unlikely, the possibility cannot be excluded that the P and N content in immature valve biosilica is derived from purely inorganic components. In future research, it will therefore be necessary to demonstrate the presence of biomacromolecules in valve SDVs through more direct methods like immunolocalization or mass spectrometry.

Methods

Chemicals and enzymes

Oligonucleotides were purchased from Eurofins Genomics. The enzymes for molecular genetics and phenylmethylsulfonyl fluoride (PMSF) were purchased from Thermo Fisher Scientific. Hydroxyethyl-piperazineethane-sulfonic acid (Hepes), sodium chloride, and sucrose were obtained from Sigma-Aldrich. Ampicillin was obtained from Merck and nourseothricin from Jena Bioscience. The TEM gold finder grids were purchased from Science Service. PDMPPO was obtained from AAT Bioquest and the sodium dodecyl sulfate (SDS) was obtained from Carl Roth. MiliQ-purified H₂O was used for all experiments.

Cell culturing

The wild type and transformant strains of *T. pseudonana* CCMP1335 and *C. cryptica* CCMP332 were maintained in artificial seawater (ASW) according to Darley and Volcani (51) with modifications as described in Supporting Information. Cells were cultured at 18 °C and 5000 lx in a 12 hours/12 hours day-night cycle.

Generating transgenic *C. cryptica* expressing ccSin1-GFP

For C-terminal *GFP*-tagging of the *ccSin1* gene (ID: g20669) the *ccSin1* promoter region (978 bp upstream of the start ATG) and the *ccSin1* coding region was amplified from genomic DNA using the sense primer 5'-ACTTGGGCCCCCTTCATGGCACCGGTGAGG-3' (*Apal* site underlined) and the antisense primer 5'-GATCCCCGGGGCCATGGCACACCCTGTC-3' (*SmaI* site underlined). The resulting PCR product was digested with *Apal* and *SmaI* and introduced into the *Apal* and *EcoRV* sites of pTpNR-GFPHpaI/fcpNat(-NotI) (52) generating pPccSin1-GFP-/fcpNAT(-NotI). The *ccSin1* terminator region (488 bp downstream of the stop codon) was amplified from genomic DNA using the sense primer 5'-ATCGCGCCCGCAGGTCATCGCTTGAGCTGGCAC-3' (*NotI* site underlined) and the antisense primer 5'-TCAGTTAACTTGACTGTCTCTCAAAGTCCAGCG-3' (*HpaI* site underlined) and introduced into the *NotI* and *HpaI* sites of pPccSin1-GFP-/fcpNAT(-NotI) generating the final expression plasmid pPccSin1-ccSin1-GFPC-TccSin1/fcpNAT(-NotI). The sequences were confirmed by DNA sequencing (Eurofins). In the plasmid expression of the *ccSin1-GFP fusion gene* is under control of the endogenous *ccSin1* regulatory sequences. The biolistic transformation of *C. cryptica* and the selection of nourseothricin resistant transformants was performed as described previously (53).

Cell synchronization, PDMPO labeling, and cell lysis

All cell density measurements were done in triplicate using the TC10™ Automated Cell Counter (Bio-Rad). Diatom cells were grown in 300 mL ASW to a cell density of $2.0\text{--}5.0 \cdot 10^5$ cells \cdot mL⁻¹. The cells were pelleted by centrifugation (3000 xg , 10 min), resuspended in 240 mL Si-free ASW, pelleted again, resuspended in 300 mL Si-free ASW, and incubated for 16 hours (12 hours dark, 4 hours light). During silicon starvation, the cell culture was in a polycarbonate flask under constant aeration. Subsequently, Na₂SiO₃ was added to the culture at a final concentration of 200 μ M, and the aeration was turned off. *T. pseudonana* and *C. cryptica* cells were incubated in constant light for 9 and 10 hours, respectively, by which time the cell density had doubled. The cells were then subjected to a second silicon starvation period by pelleting 150 mL of the cell culture, washing the cells with Si-free ASW as above, and the resuspension in 300 mL Si-free ASW. The cell culture was incubated for 16 hours (12 hours dark, 4 hours light) under constant aeration in a polycarbonate flask. Subsequently, Na₂SiO₃ was added to the cell culture at a final concentration of 200 μ M and the aeration was stopped. Three hours (*T. pseudonana*) or 5.5 hours (*C. cryptica*) after Na₂SiO₃ addition, the entire cell culture was centrifuged at 3000 xg for 10 min, resuspended in 30 mL ASW, and PDMPO was added to a final concentration of 1 μ M. After 10 min incubation under constant light, the cells were centrifuged (3000 xg , 10 min) and the pellet was resuspended in 6 ml of lysis buffer (50 mM Hepes \cdot NaOH pH 7.5, 150 mM NaCl, 50 mM Sucrose, 100 μ M PMSF). The cell suspension was distributed in 750 μ l aliquots into eight 2 ml eppendorf tubes, and 300 μ L of nitric acid-cleaned glass beads (\emptyset 0.2 mm, Retsch) were added. The cells were vigorously vortexed 3 times for 30 s each, the supernatants were transferred into a fresh tube and kept on ice until further use.

Confocal fluorescence microscopy

For imaging, 10 μ l of a cell suspension or cell lysate were spotted onto a 22 mm x 50 mm coverslip and overlaid with a thin agarose slice (1% in ASW medium). A Zeiss LSM780 inverted confocal microscope with a Zeiss Plan-Apochromat 63 \times (1.4) oil DIC M27 objective was used for image acquisition. GFP and chloroplast autofluorescence were excited with a 488 nm laser line (power set to 1.0%), a MBS 488 beam splitter, and a 32-channel GaAsP spectral detector. Two channels were used to image GFP (491–535 nm) separated from chloroplast autofluorescence (655–721 nm).

Alignment of fluorescence and electron microscopy

A 10 μ l drop of the cell lysate was spotted on a Formvar-coated gold finder grid for 1 hour. The grid was washed 3 times with lysis buffer (50 mM Hepes pH 7.5, 150 mM NaCl, 50 mM Sucrose, 100 μ M PMSF) and placed on a glass slide with the sample facing up. The locations of valve SDVs on the grid were identified by PDMPO fluorescence using a 63x oil objective on a Zeiss Axiovert 200 inverted microscope equipped with a PDMPO filter (excitation 365–395 nm, emission 530–535 nm). Images of the fluorescent valve SDVs with nearby grid bars or letters were taken to document the location for electron microscopy. The grid was then washed 3 times with water and dried by removing the majority of the water with a piece of filter paper followed by air drying overnight. For electron microscopy, the grids were analyzed

using a Morgagni 268D (FEI) instrument at an acceleration voltage of 80 kV. SDV positions were identified using the position information from the fluorescence microscopy.

Stem-edx Measurements On Valve Sdvs

Valve SDVs were localized on a formvar-coated gold grid as described above. Early valve SDVs with associated nanoparticles were analyzed using EDX spectroscopy. The local elemental concentrations have been analyzed using a JEOL JEM-F200 operated at 200 kV equipped with a dual 100 mm² windowless silicon drift detector. Scanning transmission electron microscope images have been acquired with a convergence semi-angle of 12 mrad. The EDX spectra have been denoised with principal component analyses (PCA) using 20 components (54).

Detergent treatment of valve SDVs for TEM-EDX analysis

Prior to immobilization on the TEM grid, the cell lysate was incubated with 2% (w/v) SDS for 20 min at room temperature. The SDS-treated lysate was immobilized on a Formvar-coated gold grid and analyzed by STEM-EDX as described above.

Abbreviations

AFM

Atomic force microscopy

ASW

Artificial seawater

DLA

Diffusion limited aggregation

EDX

Energy dispersive x-ray spectroscopy

EF

Epifluorescence microscopy

GFP

green fluorescent protein

Hepes

Hydroxyethyl-piperazineethane-sulfonic acid

keV

Kilo electron volt

LCPA

Long chain polyamines

PCA

Principal component analyses

PCR
Polymerase chain reaction
PDMPO
2-(4-pyridyl)-5-((4-(2- dimethylaminoethylaminocarbonyl)methoxy)phenyl)oxazole
PMSF
phenylmethylsulfonyl fluoride
SDS
Sodium dodecyl sulfate
SDV
silica deposition vesicle
SEM
Scanning electron microscopy
Sin1
Silicanin-1
STEM
Scanning transmission electron microscopy
TEM
Transmission electron microscopy

Declarations

Availability of data and materials

The authors declare that all data supporting the findings of this study are available within the article and its supplementary information or are available from the corresponding author upon request. The source data for Fig. 1C, D are available as Supporting data 1.

Competing interests

The authors declare that they have no competing interests.

Funding

This work was funded by the Deutsche Forschungsgemeinschaft (DFG) through Research Unit 2038 “NANOMEE” (DFG grant KR 1853/6 – 2), which provided the resources for the design of the study as well as collection, analysis, and interpretation of the data.

Author's contributions

NK and CH conceived the project, designed experiments, analysed data, and wrote the paper. CH and JH performed experiments. PF designed experiments and analyzed data. DP performed experiments and analysed data. BR supervised the STEM/EDX data analysis. All authors have read and approved the manuscript.

Acknowledgements

We are indebted to Paul Bomans and Nico Sommerdijk (Eindhoven Institute of Technology, The Netherlands) for initial help with elemental analysis of valve SDVs, Jennifer Klemm (TU Dresden) for help with *C. cryptica* transformation, Damian Pawolski (TU Dresden) for help with TEM analysis, Alexander Kotzsch (TU Dresden) for confocal microscopy analysis, and Nicole Poulsen (TU Dresden) for designing the ccSin1-GFP expression vector and critically reading the manuscript,. Expert support was provided by the Light Microscopy Facility and the Electron Microscopy Facility of the Center for Cellular and Molecular Bioengineering (TU Dresden).

References

1. Raven JA. The Transport and Function of Silicon in Plants. *Biol Rev.* 1983;58(2):179–207.
2. Assmy P, Smetacek V, Montresor M, Klaas C, Henjes J, Strass VH, et al. Thick-shelled, grazer-protected diatoms decouple ocean carbon and silicon cycles in the iron-limited Antarctic Circumpolar Current. *Proc Natl Acad Sci U S A.* 2013;110(51):20633–8.
3. De Tommasi E, Gielis J, Rogato A. Diatom Frustule Morphogenesis and Function: a Multidisciplinary Survey. *Mar Genomics.* 2017;35(October):1–18.
4. Parkinson J, Gordon R. Beyond micromachining: the potential of diatoms. *Trends Biotechnol.* 1999;17(5):190–6.
5. Nassif N, Livage J. From diatoms to silica-based biohybrids. *Chem Soc Rev.* 2011;40(2):849–59.
6. Gordon R, Losic D, Tiffany MA, Nagy SS, Sterrenburg FAS. The Glass Menagerie: diatoms for novel applications in nanotechnology. *Trends Biotechnol.* 2009;27(2):116–27.
7. Kröger N, Brunner E. Complex-shaped microbial biominerals for nanotechnology. *Wiley Interdiscip Rev Nanomedicine Nanobiotechnology.* 2014;6(6):615–27.
8. Losic D, Mitchell JG, Voelcker NH. Diatomaceous lessons in nanotechnology and advanced materials. *Adv Mater.* 2009;21(29):2947–58.
9. Jeffryes C, Campbell J, Li H, Jiao J, Rorrer G. The potential of diatom nanobiotechnology for applications in solar cells, batteries, and electroluminescent devices. *Energy Environ Sci.* 2011;4(10):3930–41.
10. Falciatore A, Jaubert M, Bouly J-P, Bailleul B, Mock T. Diatom Molecular Research Comes of Age: Model Species for Studying Phytoplankton Biology and Diversity. *Plant Cell.* 2020;32:547–57.

11. Delalat B, Sheppard VC, Rasi Ghaemi S, Rao S, Prestidge CA, McPhee G, et al. Targeted drug delivery using genetically engineered diatom biosilica. *Nat Commun.* 2015;6(8791).
12. Hildebrand M, Lerch SJL, Shrestha RP. Understanding diatom cell wall silicification-moving forward. *Front Mar Sci.* 2018;5:1–19.
13. Pickett-Heaps JD, Schmid AMM, Edgar LA. The cell biology of diatom valve formation. *Progr Phycol Res.* 1990;7:1–168.
14. Losic D. *Diatom Nanotechnology: Progress and Emerging Applications.* 1st ed. Royal Society of Chemistry; 2017.
15. Tesson B, Hildebrand M. Extensive and Intimate Association of the Cytoskeleton with Forming Silica in Diatoms: Control over Patterning on the Meso- and Micro-Scale. *PLoS One.* 2010;5(12).
16. Schmid AMM. Aspects of morphogenesis and function of diatom cell walls with implications for taxonomy. *Protoplasma.* 1994;181(1–4):43–60.
17. Sumper M, Brunner E. Silica biomineralisation in diatoms: The model organism *Thalassiosira pseudonana*. *ChemBioChem.* 2008;9(8):1187–94.
18. Chiovitti A, Harper RE, Willis A, Bacic A, Mulvaney P, Wetherbee R. Variations in the substituted 3-linked mannans closely associated with the silicified walls of diatoms. *J Phycol.* 2005;41(6):1154–61.
19. Kröger N, Poulsen N. Diatoms-from cell wall biogenesis to nanotechnology. *Annu Rev Genet.* 2008;42:83–107.
20. Poulsen N, Sumper M, Kröger N. Biosilica formation in diatoms: Characterization of native silaffin-2 and its role in silica morphogenesis. *Proc Natl Acad Sci.* 2003;100(21):12075–80.
21. Poulsen N, Kröger N. Silica morphogenesis by alternative processing of silaffins in the diatom *Thalassiosira pseudonana*. *J Biol Chem.* 2004;279(41):42993–9.
22. Pawolski D, Heintze C, Mey I, Steinem C, Kröger N. Reconstituting the formation of hierarchically porous silica patterns using diatom biomolecules. *J Struct Biol.* 2018;204(1):64–74.
23. Gordon RM, Drum RW. The chemical basis of diatom morphogenesis. *Int Rev Cytol.* 1994;150:243–372.
24. Parkinson J, Brechet Y, Gordon R. Centric diatom morphogenesis: A model based on a DLA algorithm investigating the potential role of microtubules. *Biochim Biophys Acta - Mol Cell Res.* 1999;1452(1):89–102.
25. Cox E, Willis L, Bentley K. Integrated simulation with experimentation is a powerful tool for understanding diatom valve morphogenesis. *Biosystems.* 2012;109(3):450–9.
26. Idei M, Sato S, Tamotsu N, Mann DG. Valve morphogenesis in *Diploneis smithii* (Bacillariophyta). *J Phycol.* 2018;54(2):171–86.
27. Cox EJ. Variation in patterns of valve morphogenesis between representatives of six biraphid diatom genera (Bacillariophyceae). *J Phycol.* 1999;35(6):1297–312.

28. Hildebrand M, York E, Kelz JI, Davis AK, Frigeri LG, Allison DP. Nanoscale control of silica morphology and three-dimensional structure during diatom cell wall formation. *J Mater Res.* 2006;21(10):2689–98.
29. Tesson B, Hildebrand M. Dynamics of silica cell wall morphogenesis in the diatom *Cyclotella cryptica*: Substructure formation and the role of microfilaments. *J Struct Biol.* 2010;169(1):62–74.
30. Schmid AMM, Schulz D. Wall morphogenesis in diatoms: Deposition of silica by cytoplasmic vesicles. *Protoplasma.* 1979;100(3–4):267–88.
31. Drum RW, Pankratz HS. Post mitotic fine structure of *Gomphonema parvulum*. *J Ultrastruct Res.* 1964;10:217–23.
32. Pickett-Heaps JD. Cell division and morphogenesis of the centric diatom *Chaetoceros decipiens* (Bacillariophyceae) II. Electron microscopy and a new paradigm for tip growth. *J Phycol.* 1998;34(6):995–1004.
33. Pickett-Heaps JD, Kowalski SE. Valve morphogenesis and the microtubule center of the diatom *Hantzschia amphioxys*. *Eur J Cell Biol.* 1981 Aug;25(1):150–70.
34. Chiappino ML, Volcani BE. Studies on the Biochemistry and Fine Structure of Silicia Shell Formation in Diatoms. *Protoplasma.* 1977;93:205–21.
35. Pickett-Heaps JD, Tippit D, Andreozzi J. Cell division in the pennate diatom *Pinnularia*. IV. Valve morphogenesis. *Biol Cell.* 1979;35(2):199–206.
36. Kröger N, Wetherbee R. Pleuralins are involved in theca differentiation in the diatom *Cylindrotheca fusiformis*. *Protist.* 2000;151(3):263–73.
37. Armbrust EV, Berges JA, Bowler C, Green BR, Martinez D, Putnam NH, et al. The genome of the diatom *Thalassiosira pseudonana*: Ecology, evolution, and metabolism. *Science.* 2004;306(5693):79–86.
38. Traller JC, Cokus SJ, Lopez DA, Gaidarenko O, Smith SR, McCrow JP, et al. Genome and methylome of the oleaginous diatom *Cyclotella cryptica* reveal genetic flexibility toward a high lipid phenotype. *Biotechnol Biofuels.* 2016;9(1):1–20.
39. Poulsen N, Chesley PM, Kröger N. Molecular genetic manipulation of the diatom *Thalassiosira pseudonana* (Bacillariophyceae). *J Phycol.* 2006;42(5):1059–65.
40. Dunahay TG, Jarvis EE, Roessler PG. Genetic Transformation of the diatoms *Cyclotella cryptica* and *Navicula saprophila*. *J Phycol.* 1995;31(6):1004–12.
41. Kotzsch A, Gröger P, Pawolski D, Bomans PHH, Sommerdijk NAJM, Schlierf M, et al. Silicanin-1 is a conserved diatom membrane protein involved in silica biomineralization. *BMC Biol.* 2017;15(65):9–11.
42. Shimizu K, Del Amo Y, Brzezinski MA, Stucky GD, Morse DE. A novel fluorescent silica tracer for biological silicification studies. *Chem Biol.* 2001;8(11):1051–60.
43. Hildebrand M, Frigeri LG, Davis AK. Synchronized Growth of *Thalassiosira pseudonana* (Bacillariophyceae) Provides Novel Insights into Cell- Wall Synthesis Processes in Relation to the Cell Cycle. 2007;43(4):730–40.

44. Kröger N, Deutzmann R, Sumper M. Polycationic Peptides from Diatom Biosilica That Direct Silica Nanosphere Formation. *Science* (80-). 1999;286(5442):1129–32.
45. Crawford SA, Higgins MJ, Mulvaney P, Wetherbee R. Nanostructure of the diatom frustule as revealed by atomic force and scanning electron microscopy. *J Phycol.* 2001;37(4):543–54.
46. Noll F, Sumper M, Hampp N. Nanostructure of Diatom Silica Surfaces and of Biomimetic Analogues. *Nano Lett.* 2002;2(2):91–5.
47. Grachev MA, Bedoshvili YD, Gerasimov EY, Zaikovskii VI, Gneusheva KV, Likhoshway YV. Silica-containing inclusions in the cytoplasm of diatom *Synedra acus*. *Dokl Biochem Biophys.* 2017;472(1):44–8.
48. Dixit S, Van Cappellen P, Bennekom AJ. Processes Controlling Solubility of Biogenic Silica and Pore Water Build-up of Silicic Acid in Marine Sediments. *Mar Chem.* 2001;73(3):333–52.
49. Machill S, Kohler L, Ueberlein S, Hedrich R, Kunaschk M, Paasch S, et al. Analytical studies on the incorporation of aluminium in the cell walls of the marine diatom *Stephanopyxis turris*. *Biometals.* 2013;26(1):141–50.
50. Lutz K, Gröger C, Sumper M, Brunner E. Biomimetic silica formation: Analysis of the phosphate-induced self-assembly of polyamines. *Phys Chem Chem Phys.* 2005;7(14):2812–5.
51. Darley WM, Volcani BE. Role of Silicon in Diatom Metabolism: A Silicon Requirement for Deoxyribonucleic Acid Synthesis in the Diatom *Cylindrotheca fusiformis*. *Exp Cell Res.* 1969;58(2):334–42.
52. Kotzsch A, Pawolski D, Milentyev A, Shevchenko A, Scheffel A, Poulsen N, et al. Biochemical composition and assembly of biosilica-associated insoluble organic matrices from the diatom *Thalassiosira pseudonana*. *J Biol Chem.* 2016;291(10):4982–97.
53. Kumari E, Görlich S, Poulsen N, Kröger N. Genetically Programmed Regioselective Immobilization of Enzymes in Biosilica Microparticles. *Adv Funct Mater.* 2020;accepted.
54. Lucas G, Burdet P, Cantoni M, Hébert C. Multivariate statistical analysis as a tool for the segmentation of 3D spectral data. *Micron.* 2013;52–53(September-October):49–56.

Figures

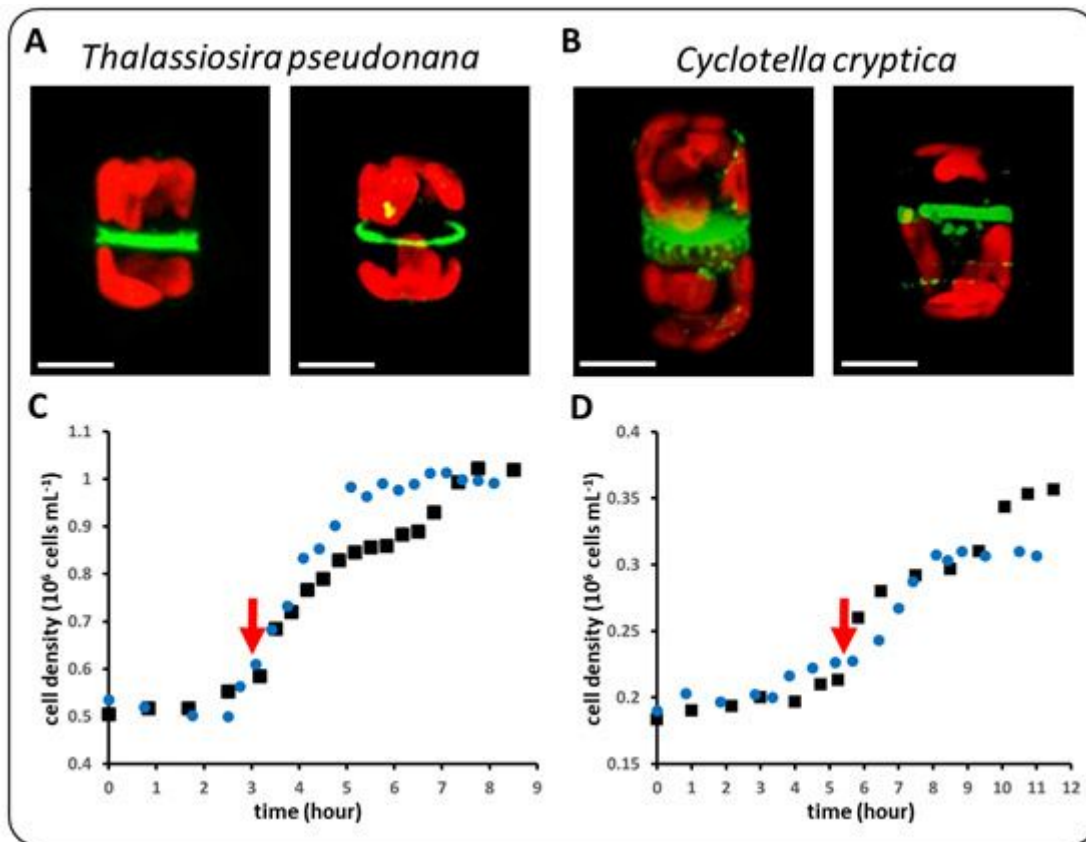


Figure 1

Live cell imaging of silicanin-1 GFP fusion proteins in individual cells of (A) *T. pseudonana* and (B) *C. cryptica*. The left panels show an individual cell after cytokinesis with one valve SDV (green, plate-like structure) in each sibling cell. The right panel shows a cell during interphase with a girdle band SDV and additional silicanin-1-GFP bearing intracellular vesicles. Green color indicates GFP fluorescence and red color shows chlorophyll autofluorescence. Scale bar: 4 μm . Cell density measurements during the first (black dots) and second (blue dots) series of Si starvation-replenishment with (C) *T. pseudonana* and (D) *C. cryptica*. The red arrow indicates the time point at which the highest proportion of dividing cells was observed in the second Si starvation-replenishment cycle. Standard deviations ($n=3$) for the first Si starvation-replenishment series were $\pm 0.07 \cdot 10^6$ cells $\cdot \text{mL}^{-1}$ (*T. pseudonana*) and $\pm 0.03 \cdot 10^6$ cells $\cdot \text{mL}^{-1}$ (*C. cryptica*), and for the second series $\pm 0.1 \cdot 10^6$ cells $\cdot \text{mL}^{-1}$ (*T. pseudonana*) and $\pm 0.04 \cdot 10^6$ cells $\cdot \text{mL}^{-1}$ (*C. cryptica*) (see Supporting Information).

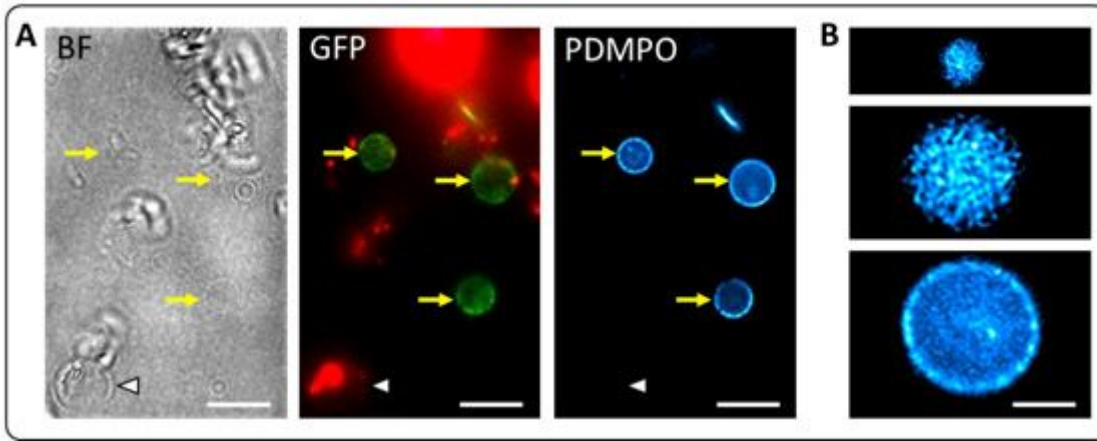


Figure 2

Identification of valve SDVs in the lysates from Sin1-GFPC expressing and PDMPO labeled *T. pseudonana* cells. (A) Bright field (BF) and epifluorescence images of the same lysate in the GFP and PDMPO channels. The red color is due to chlorophyll autofluorescence. Yellow arrows point to valve SDVs. The white arrowhead points to a mature valve with neither GFP nor PDMPO fluorescence. Scale bars: 10 μ m. (B) PDMPO fluorescence patterns of three individual valve SDVs from a cell lysate. Scale bar: 3 μ m (all images have the same magnification).

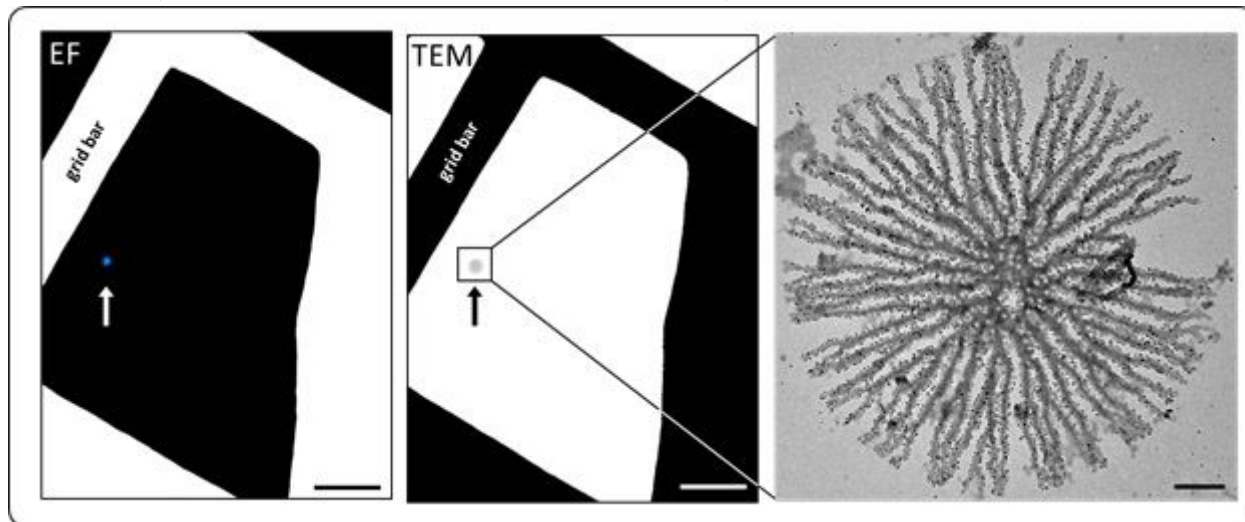


Figure 3

Correlative fluorescence and electron microscopy of a valve SDV (arrow). A PDMPO labeled valve SDV was identified by epifluorescence microscopy (EF) on a finder grid and subsequently analyzed with TEM (middle and right images). Scale bars: 10 μ m (left and middle images), 400 nm (right image).

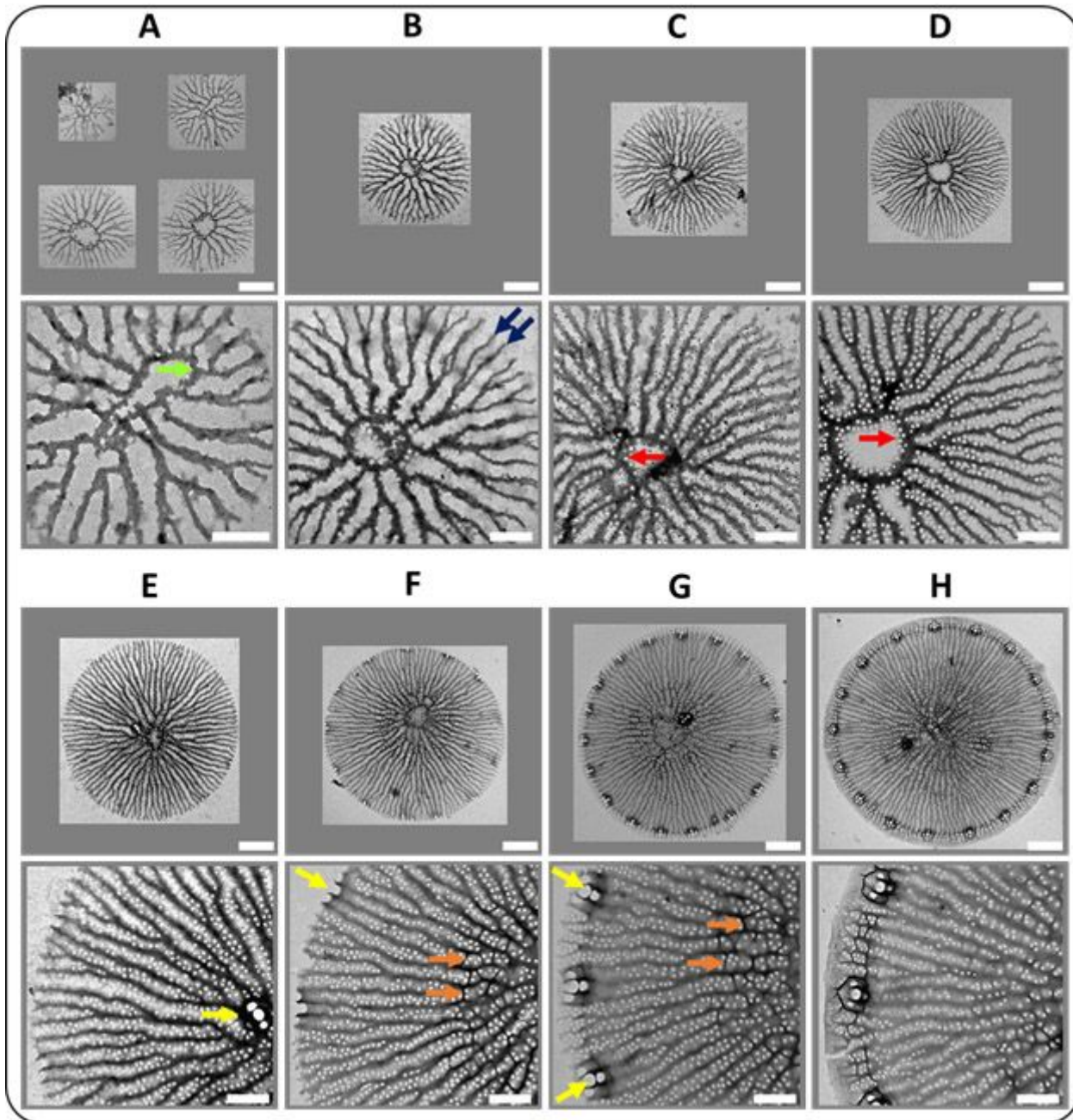


Figure 4

Valve development in *T. pseudonana*. Different valve SDVs were imaged by TEM and ordered based on the stage of silica structure formation. For each valve, an overview image (top row) and a corresponding detail image (bottom row) is shown. Colored arrows highlight characteristic biosilica features: green = annulus, blue = costa, red = cribrum pore, yellow = fultoportula, orange = areola pore. Scale bars: 1 μm (overview images), 400 nm (detail images).

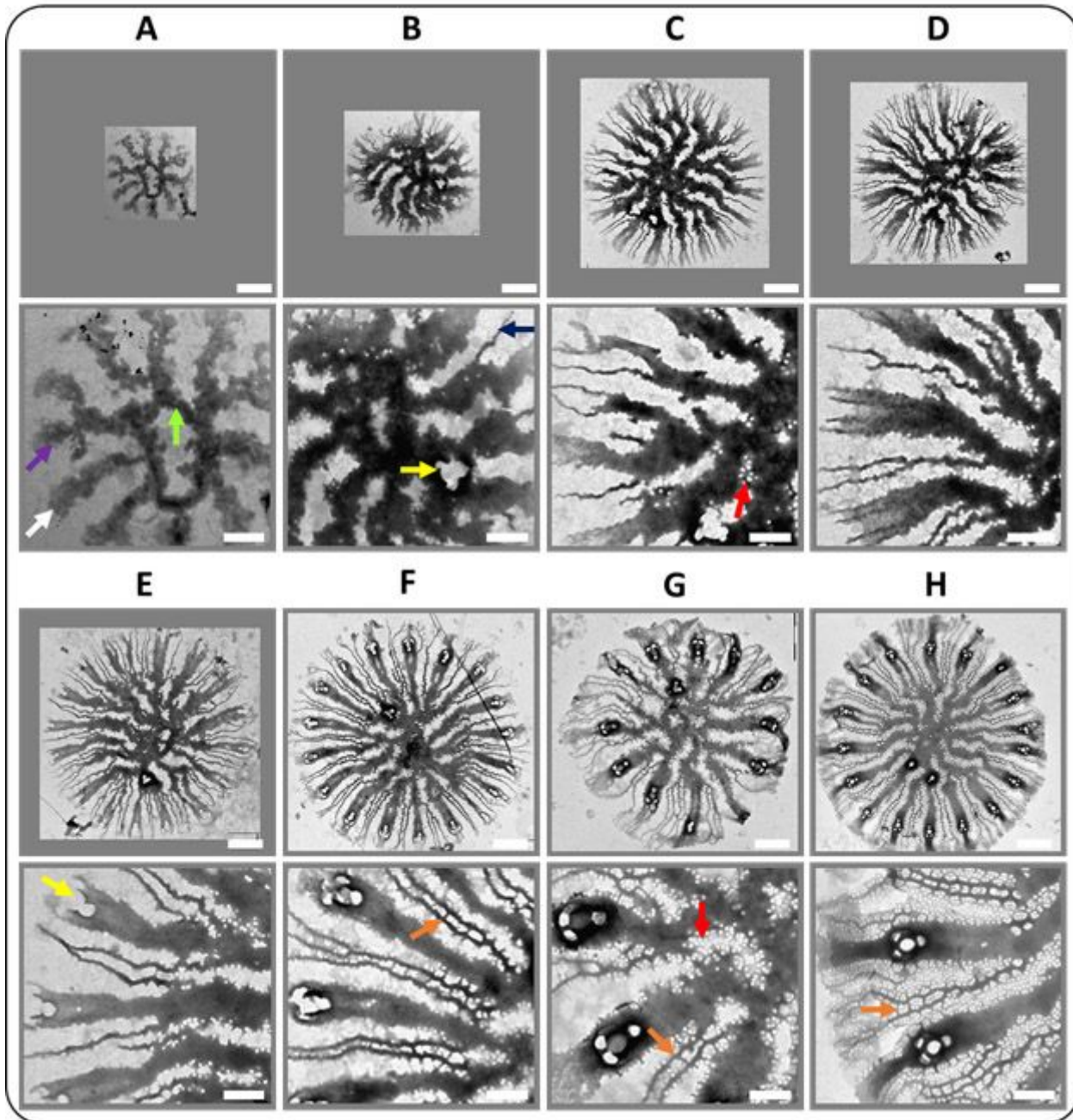


Figure 5

Valve development in *C. cryptica*. Different valve SDVs were imaged by TEM and ordered based on the stage of silica structure formation. For each valve an overview image (top row) and a corresponding detail image (bottom row) is shown. Colored arrows highlight characteristic biosilica features: green = annulus, purple = wide costa, blue = narrow costae, red = cribrum pore, yellow = fultoportula, orange = areola pore. Scale bars: 1 μm (overview images), 400 nm (detail images).

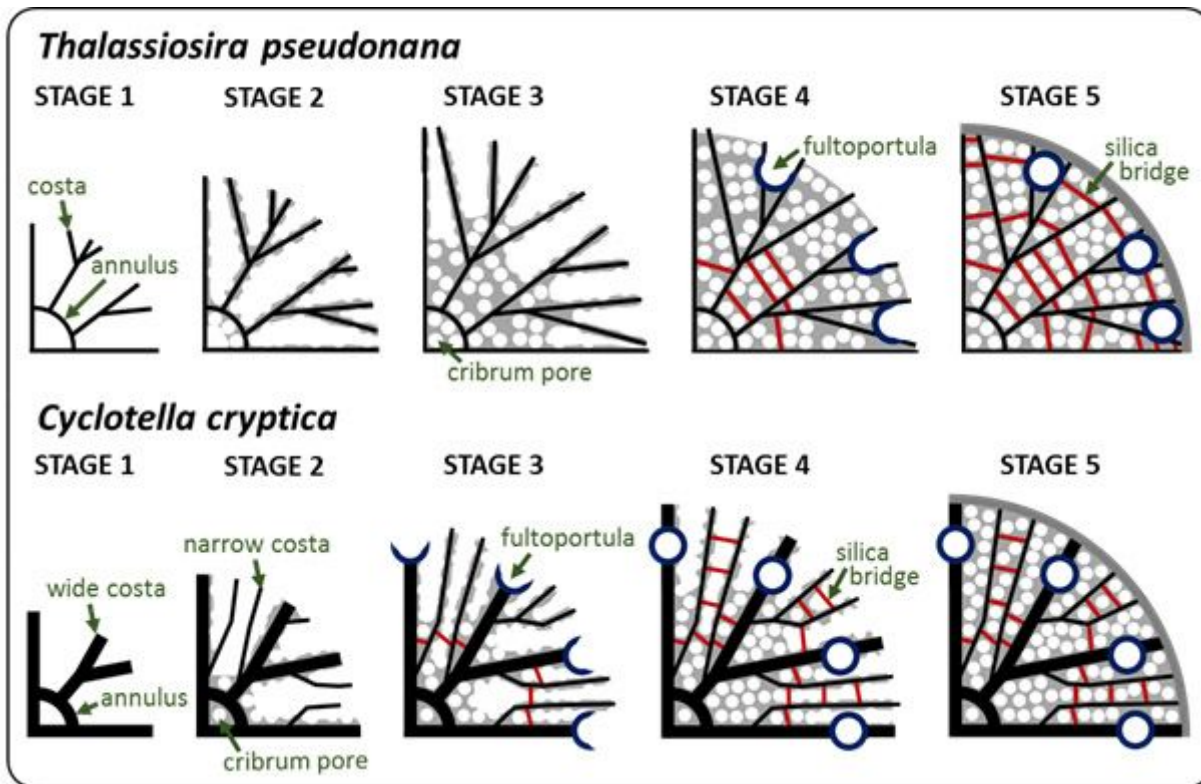


Figure 6

Schematics of valve morphogenesis in *T. pseudonana* and *C. cryptica*. Morphogenesis proceeds from left to right. For simplicity only a quarter of the developing valves are shown.

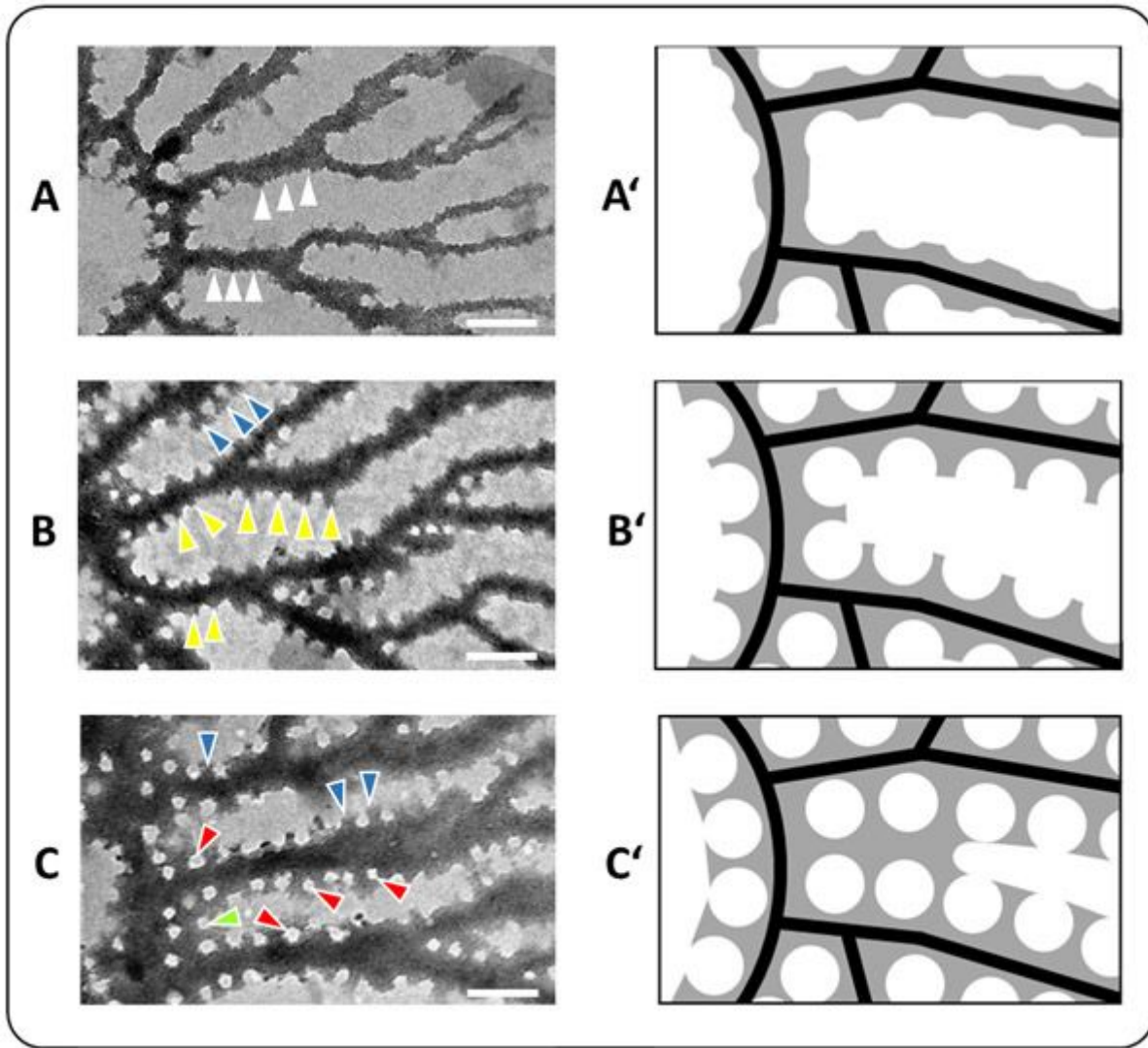


Figure 7

Morphogenesis of cribrum pores in *T. pseudonana*. Images (A-C) show TEM micrographs from valve SDVs in different developmental stages, and images (A'-C') show schematics of the same developmental stages. The arrows point to characteristic intermediate stages of pore development. The arrowheads point to features that are described in the text. Scale bars: 200 nm.

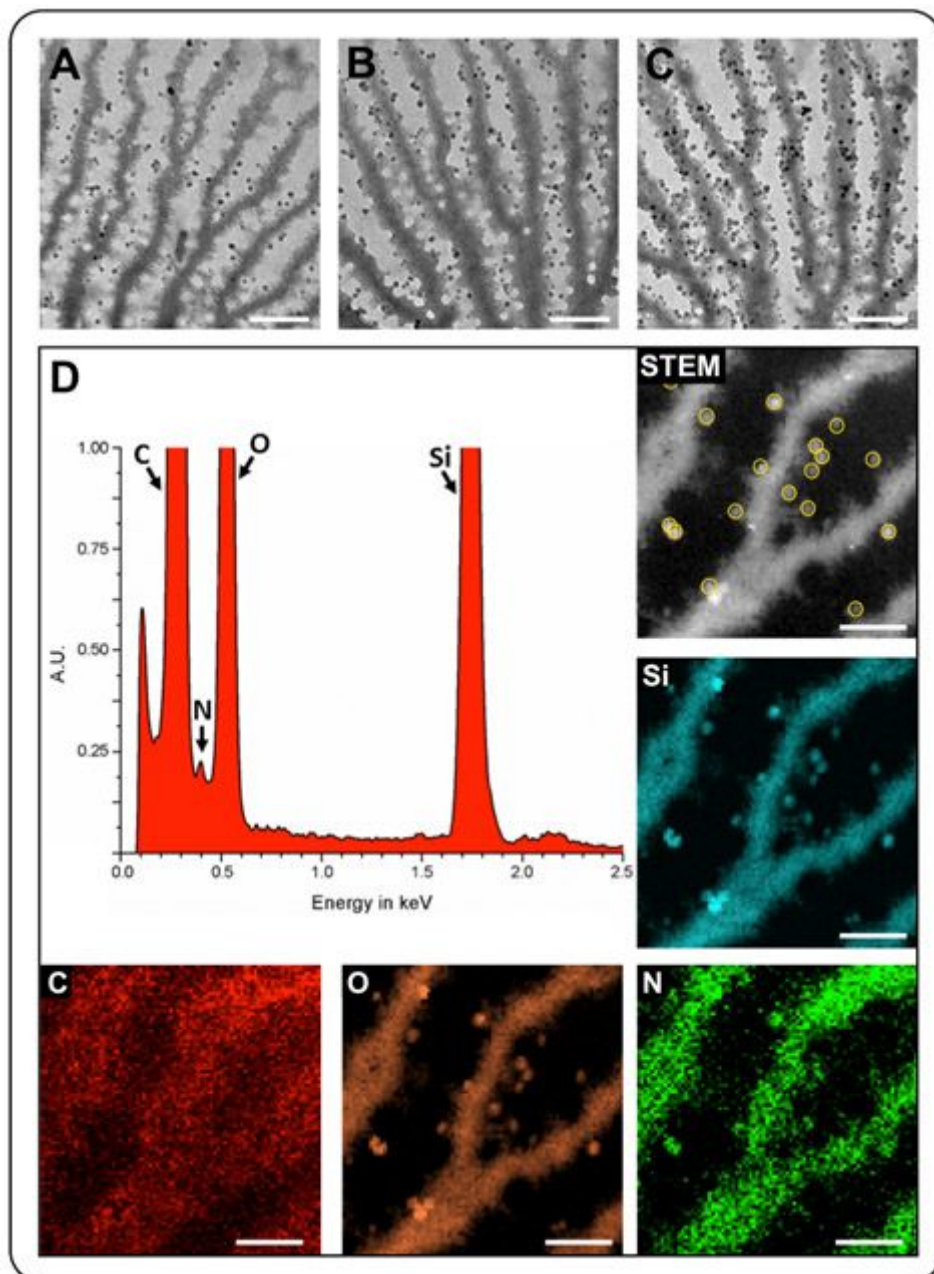


Figure 8

(A-C) TEM images of early valve SDVs with associated ~ 20 nm sized spherical nanoparticles. Scale bars: 200 nm. (D) Scanning transmission electron microscopy (STEM) EDX analysis of several nanoparticles within a single valve SDV. The yellow circles in the STEM image highlight the nanoparticles from which the EDX spectrum was obtained. The elemental maps are depicted with the corresponding chemical symbol. Scale bars: 100 nm.

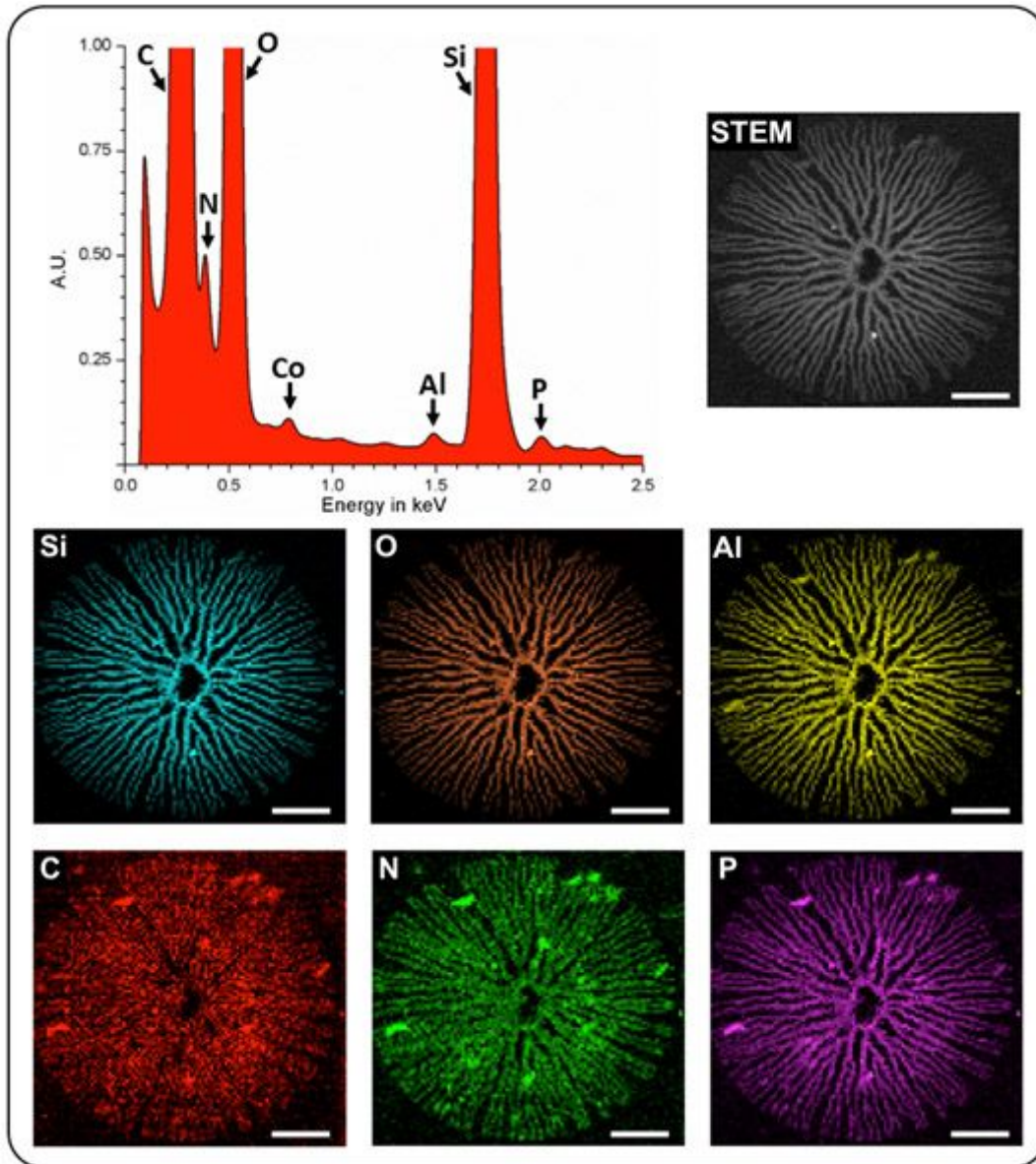


Figure 9

EDX analysis of an SDS-extracted, immature valve from *T. pseudonana*. The STEM image of the valve is shown on the upper right. The EDX spectrum is derived from the entire valve surface. The elemental maps are depicted with the corresponding chemical symbol. Scale bars: 100 nm.

Supplementary Files

This is a list of supplementary files associated with this preprint. Click to download.

- [SupplementaryFile.docx](#)
- [SourceFile1.xlsx](#)